Electronic supplementary information for

1D/3D hierarchical carbon skeleton confined NiFe nanoparticles with optimized three-phase interfaces as tri-functional electrocatalyst

*Yuqing Chen,[a] Binyang Liu,[a] Xuesong Liu,[a] Jiahui Ye,[a] Kuan Deng,[a] Chengjie Wu,[a] Qiang Niu,[b] Tao Yang,[b] Wen Tian,[a] Junyi Ji,[a,]**

[a.] School of Chemical Engineering, State Key Laboratory of Polymer Materials Engineering, Sichuan University, Chengdu 610065, P. R. China

[b] School of Biology and Chemical Engineering, Panzhihua University, Panzhihua, Sichuan, 617000, P. R. China

Corresponding author

Junyi Ji, E-mail: junyiji@scu.edu.cn

S1 Chemicals and materials

3-Aminophenol (3-AP, AR 98%), Iron sulfate heptahydrate ($FeSO_4·7H_2O$, AR 99%) and potassium hydroxide (KOH, AR 95%) are purchased from Aladdin. Nickle nitrate hexahydrate ($Ni(NO_3)·6H_2O$, AR 98%), thiourea (CH_4N_2S, AR 99%), formaldehyde solution (HCHO, AR 37%), Urea (H_2NCONH_2, AR), anhydrous ethanol (CH_3CH_2OH, AR 99%), and hydrochloric acid (HCl, AR 35-37%) are purchased from Chengdu Chron Chemicals Co., Ltd. Nafion perfluorinated resin ($C_9HF_{17}O_5S$, D520, 5 wt.%) Nickel foam (NF, 99.8%) was purchased from Chengdu Taiyu Gas Co., Ltd. The commercial IrO_2/Ti electrode is purchased from Kunshan Yiwanlin Electronic Technology Co., Ltd. for electrochemical tests. The commercial 20% Pt/C electrode is purchased from Adamas for electrochemical tests. All chemical reagents in the experiment are utilized directly without purification.

S2 Experiment

1. Synthesis of N-doped hollow carbon spheres (HCS)

The prepared APF microspheres were directly annealed in an Ar atmosphere heated to 800 °C for 2 h to prepare HCS.

2. Synthesis of HCS@Ni-350

HCS@Ni-350 was prepared by reducing APF/Ni at 350 °C in a hydrogen atmosphere. The APF/Ni microspheres are reduced at 350 °C for 3.5 h under 10% H_2/Ar atmosphere, and then the warming procedure is stopped and cooled to room temperature to prepare the HCS@Ni-350.

3. Synthesis of HCS@Ni-800

HCS@Ni-800 was prepared by direct carbonization of APF/Ni. APF/Ni microspheres were carbonized directly under Ar atmosphere at 800 °C for 2 h, then the heating procedure was stopped and cooled to room temperature to prepare HCS@Ni-800.

4. Synthesis of N-HCS@Ni-x-y

N-HCS@Ni-x-y were prepared by varying the amount of Ni^{2+} solution added to N-HCS@Ni and the C_2H_2 treatment time. The preparation of N-HCS@Ni-x-y was similar to that of N-HCS@Ni, varying the amount of infiltration solution (150 μL and 300 μL) the treatment time of C_2H_2 (5, 10, and 15 min) to prepare N-HCS@Ni-x-y (x=150 and 300 μL; y = 5, 10, and 15 min).

5. N-HCS@Ni-800 CVD

N-HCS@Ni-800 was prepared by high temperature CVD treatment. HCS@Ni was placed under a of 10% H_2/Ar in the furnace and is heated to 800 °C in 15 min. After that, the C_2H_2 (1 sccm) was introduced to grow carbon nanotubes for 1 h. And then the heating procedure was stopped and cooled to room temperature to prepare N-HCS@Ni-

with high-temperature CVD.

S3 Materials Characterization

The morphology and microstructure of the catalysts were characterized by scanning electron microscope (SEM, JEOL JSM7610F), energy dispersive X-ray spectroscopy (EDS), and transmission electron microscopy (TEM, FEI Tecnai G20). The crystalline structures and chemical valence states were identified by X-ray diffraction (XRD, Cu Kα radiation, DX2700, Dandong Haoyuan) and X-ray photoelectron spectroscopy (XPS, PHI5000 Versa spectrometer). The Raman was performed using a DXRxi spectrometer (Thermal Scientific, 455 nm).

The optical photographs of bubble generation presented in Fig. 5a and 5b were obtained by coating the samples with Ti foam. The water contact angle illustrated in Fig. 5c was determined by loading the samples on double-sided tape.

S4 Electrochemical measurement

1. OER and UOR measurement

A three-electrode configuration was employed, including a working electrode (the prepared materials), reference electrode (saturated Hg/HgO), and a counter electrode (graphite rod). The electrochemical characterizations were conducted in an electrolyte of 1 M KOH (pH = 14). The relevant RHE potential was calculated following the Nernst equation: $E_{RHE} = E_{Hg/HgO} + 0.059 \times pH + 0.098$ V. All electrochemical curves were recorded after activating the catalysts with cyclic voltammetry (CV) at a scan rate of 50 $mV \cdot s^{-1}$ (0.924 –1.624 V vs. RHE for OER and UOR) until a stable state was reached.

To observe the change of redox peak in the process of polarization, OER and UOR activity was assessed by CV at a scan rate of 2 $mV \cdot s^{-1}$ with iR correction. The overpotential (η) for OER was calculated by $\eta_{OER} = E_{RHE}$ - 1.23 V, while E_{RHE} was obtained from the cathode polarization curve. The correction is carried out in accordance with $E=E_{RHE}$-IR, where I is the corresponding current and R is the solution resistance obtained in the EIS figure.

The Tafel plots were obtained by plotting as overpotential (η) versus the logarithm of current density (log *j*) based on polarization curves.

The Tafel slope is obtained by fitting the LSV (CV) curve as $\eta = a + b \cdot \log j$, η is the reversible hydrogen electrode potential, j is the current density, and b is the Tafel slope.

Electrochemical impedance spectroscopy (EIS) was tested from 0.1 Hz to 100 kHz at an overpotential of 330 mV (vs. RHE) for OER and UOR.

Assessment of turnover frequency (TOF): TOF (s^{-1}) was calculated as follows:

$$TOF = \frac{I}{\alpha F n}$$

While I is the corresponding current (A) at a specific potential in the LSV curve, α is the number of electrons transferred by the half-reaction (OER: α = 4), F is the Faraday constant (96485 C mol^{-1}), n is the number of active sites.

The number of active sites was determined by the CV curves recorded between –0.2 and 0.6 V (vs. RHE) in PBS buffer solution (pH = 7.4) at a scan rate of 50 $mV \cdot s^{-1}$.

The number of active sites (n) was calculated at non-Faradaic regions according to the following equation:

$$n = \frac{Q}{\alpha F}$$

Where Q is the amount of charge transferred during the CV test.

The electrochemical active area (ECSA) was calculated according to following equation:

$$ECSA = \frac{C_{dl}}{C_s}$$

C_s is the specific capacitance in an alkaline electrolyte and C_{dl} is obtained from the cyclic voltammetry within the non-Faradaic region at different scan rates. C_s = 0.04 mF·cm^{-2}.[1] The C_{dl} value equals the slope of the linear relationship between the scan rate and current density. The measured sweep speed was 10-100 mV·s^{-1} and the CV measurement potential windows were 0.924 - 1.024 (vs. RHE) for OER and UOR:

The long-term stability was tested by the timed-current method.

2. ORR measurement

Catalyst inks were prepared in the same way as OER and UOR. The OER and UOR catalyst loading was 0.83 mg·cm^{-2}. A rotating disk electrode (RDE, 5 mm diameter, effective area of 0.196 cm^2) was used as working electrode. Next, 15 μL of the catalyst ink was dropped onto the surface of the RDE (Sample loading ≈ 0.43 mg·cm^{-2}).

ORR experiments were performed with a CHI 760E electrochemical workstation (CH Instruments, Inc.) at room temperature unless stated otherwise. A three-electrode configuration was employed, including a working electrode (the prepared materials), reference electrode (saturated Ag/AgCl), and a counter electrode (graphite rod). The electrochemical characterizations were conducted in an electrolyte of 0.1 M KOH (pH = 13). The relevant RHE potential was calculated following the Nernst equation: $E_{RHE} = E_{Ag/AgCl} + 0.059 \times pH + 0.197$ V. All electrochemical curves were recorded after activating the catalysts with cyclic voltammetry (CV) at a scan rate of 50 mV·s^{-1} (0.4 – 1.2 V vs. RHE for ORR) until a stable state was reached.

Before ORR tests, the 0.1 M KOH solution was saturated with O_2 by bubbling O_2 into the cell for 30 min. The ORR activities of all materials were investigated by linear sweeping voltammetry (LSV) and the cyclic voltammetry (CV) measurements, which were conducted in O_2- and N_2-saturated electrolyte from 1.2 to 0.4 V vs. RHE with a scan rate of 10 mV·s^{-1} and 50 mV·s^{-1}, respectively. The apparent electron transfer number was calculated by the Koutecky-Levich (K-L) equation at various potentials as follows:

$$\frac{1}{j}=\frac{1}{j_L}+\frac{1}{j_K}=\frac{1}{B\omega^{1/2}}+\frac{1}{j_K}$$

$$B=0.62nFC_0(D_0)^{\frac{2}{3}}\upsilon^{-\frac{1}{6}}$$

$$j_K=nFC_0$$

where j is the measured current density, j_K and j_L are the kinetic and limiting current densities, respectively, ω is the rotating speed, n is the electron transfer number, F is the Faraday constant (96485 C·mol^{-1}), C_0 is the bulk concentration of O_2 (1.2×10^{-3} mol·L^{-1}), D_0 is the diffusion coefficient of O_2 (1.9×10^{-5} cm^2 s^{-1}), and υ is the kinematic viscosity of the electrolyte (0.01 cm^2·s^{-1}).

The stability was tested by the chronoamperometry method (i - t) at half wave potential and accelerated durability test (ADT).

S5 Supporting Figures

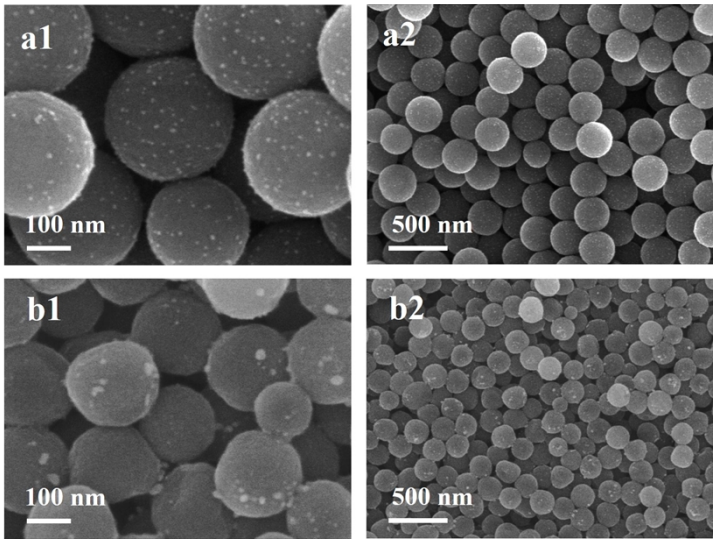

Fig. S1 (a1-2) SEM of HCS@Ni-800 with only 800 °C carbonization; (b1-2) HCS@Ni-350 with 350 °C hydrogen reduction and without 800 °C carbonization.

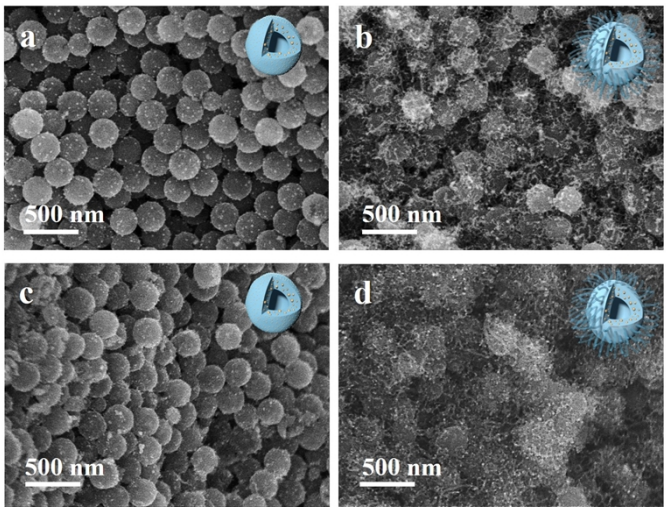

Fig. S2 The SEM images of (a) HCS@Ni; (b) N-HCS@Ni; (c) HCS@NiFe; (d) N-HCS@NiFe.

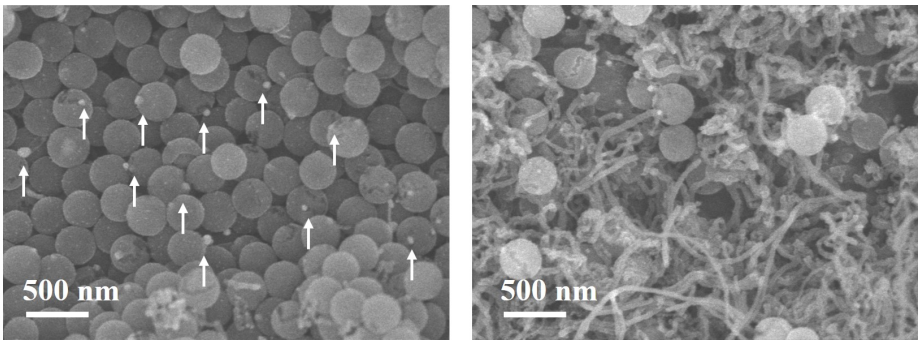

Fig. S3 SEM of N-HCS@Ni-800 with high temperature CVD treatment.

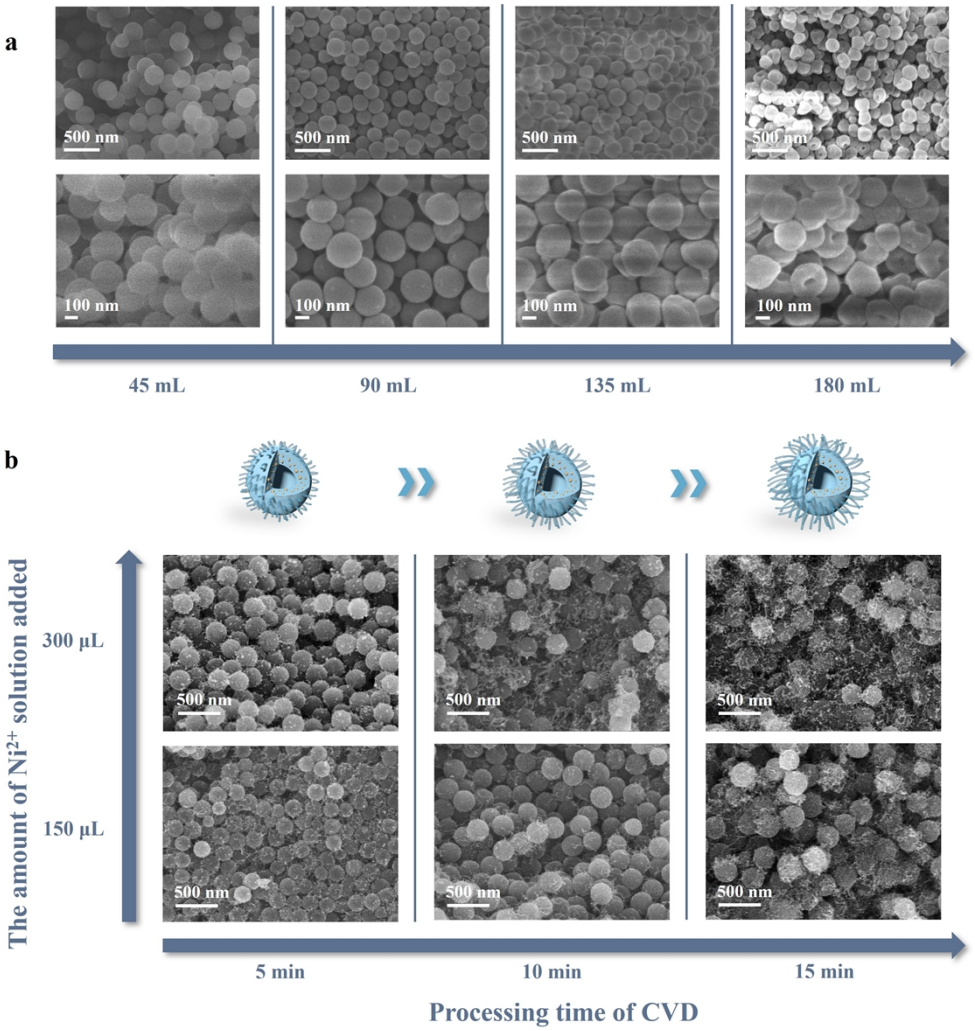

Fig. S4 SEM of (a) APF with ethanol volume; (b) N-HCS@Ni-x-y with the amount of Ni^{2+} solution and the C_2H_2 treatment time.

At the initial stage of precursor polymerization, the addition reaction of phenol formaldehyde and amino aldehyde in the lotion droplets is followed by instant condensation to quickly form oligomers. Subsequently, spatial effects promote the preferential reaction of residual substrates with oligomers on the droplet surface, forming resin spheres with uneven polymerization degree from shell to core layer. Meanwhile, the obtained resin inside the core with relatively low polymerization degree is partially soluble in ethanol. By adjusting the amount of ethanol added and utilizing the rapid interaction between short chain oligomers and ethanol increments, the thickness of the APF sphere shell can be controlled to induce varying degrees of surface

roughness (**Fig. S4a**). With the addition of larger amount of ethonol, the surface of APF sphere reveals an obvious wrinkle or even collaps nature, demonstrating the gradually thinning of the shell thickness. Considering the correlation between the shell thickness of the precursor and the properties/stability of the embedded metal, the addition amount of 90 mL of ethanol is chosen for further experiment in this study. Under this specific ethanol concentration condition, it was observed that the APF sphere shell exhibited a certain degree of local indentation. Furthermore, in the process of Ni salt impregnation and CVD growth of CNTs, we can effectively control the length and size of CNTs by precisely adjusting the CVD reaction time and the dosage of metal precursors (**Fig. S4b**).

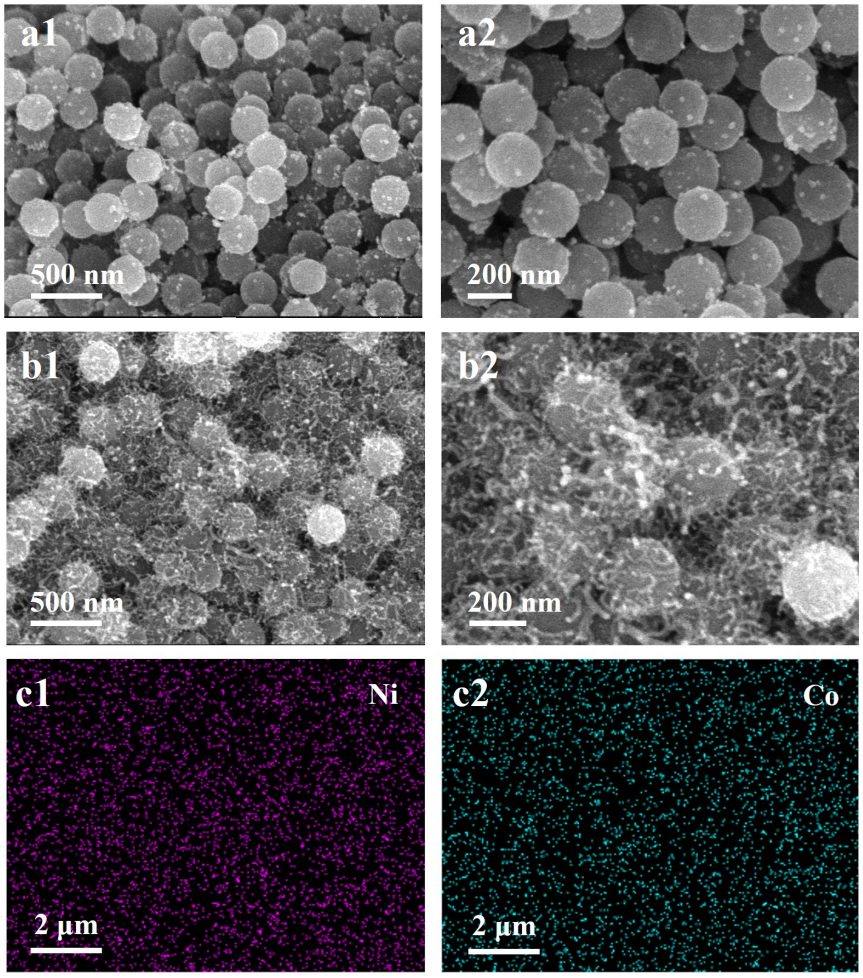

Fig. S5 SEM of (a1-2) HCS@NiCo; (b1-2) N-HCS@NiCo, (c1-2) EDS mapping of N-HCS@NiCo.

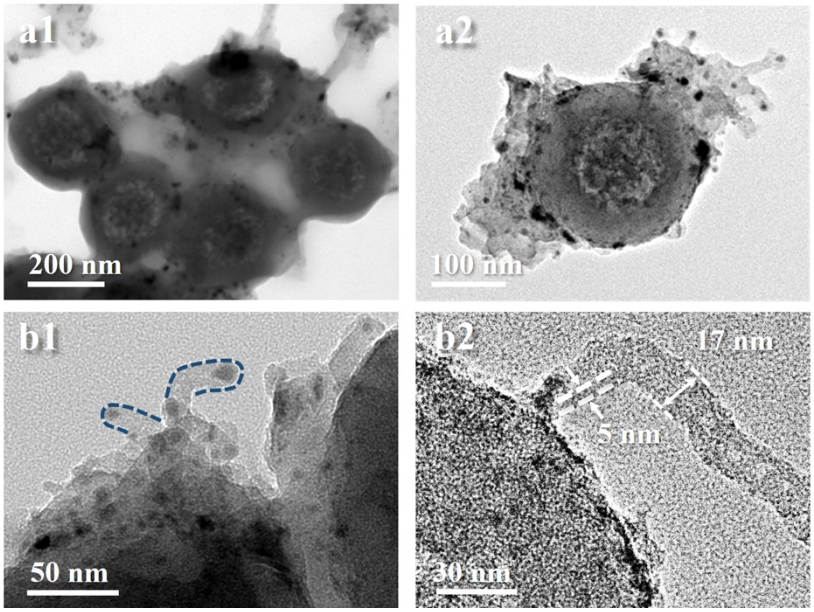

Fig. S6 Supplementary TEM images of N-HCS@NiFe.

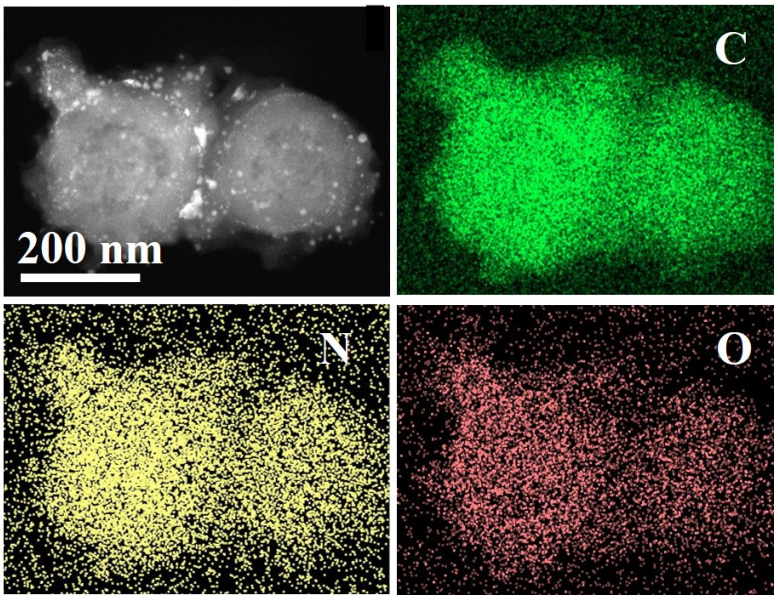

Fig. S7 TEM image and corresponding EDS mapping of C, S, O of N-HCS@NiFe.

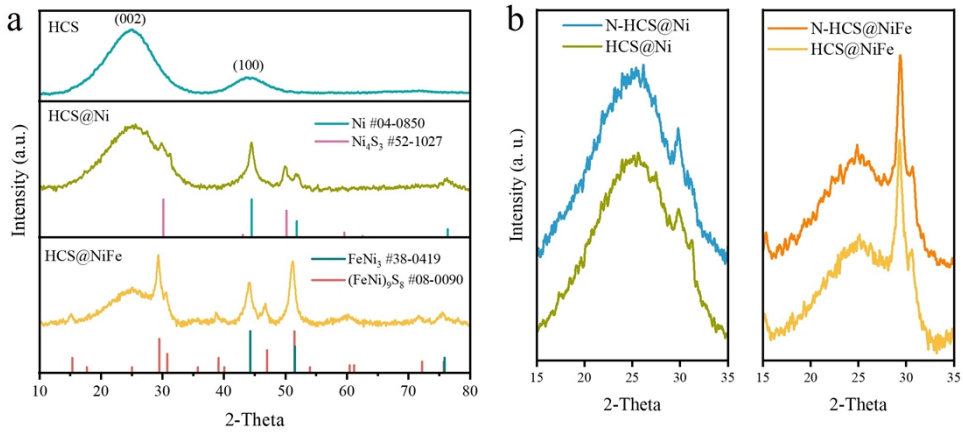

Fig. S8 (a) XRD patterns of HCS, HCS@Ni, and HCS@NiFe; (b) the comparative analysis of the diffractograms of N-HCS@Ni and HCS@Ni, N-HCS@NiFe and HCS@NiFe from 15° to 35°.

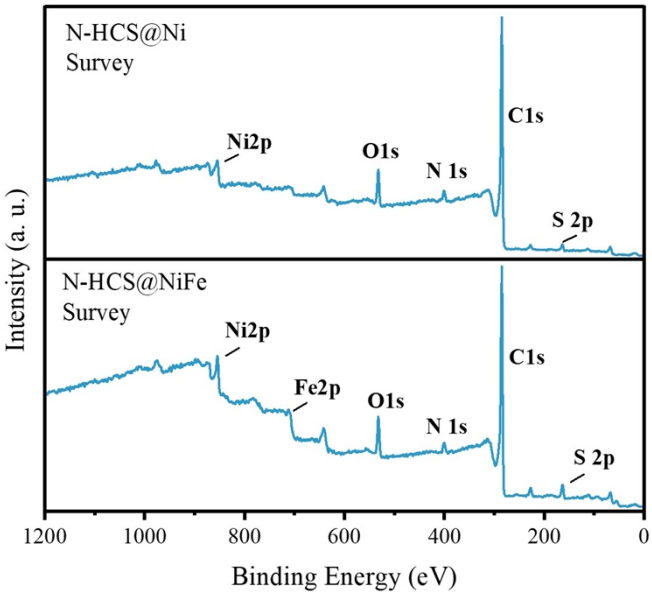

Fig. S9 The XPS full survey of N-HCS@Ni and N-HCS@NiFe.

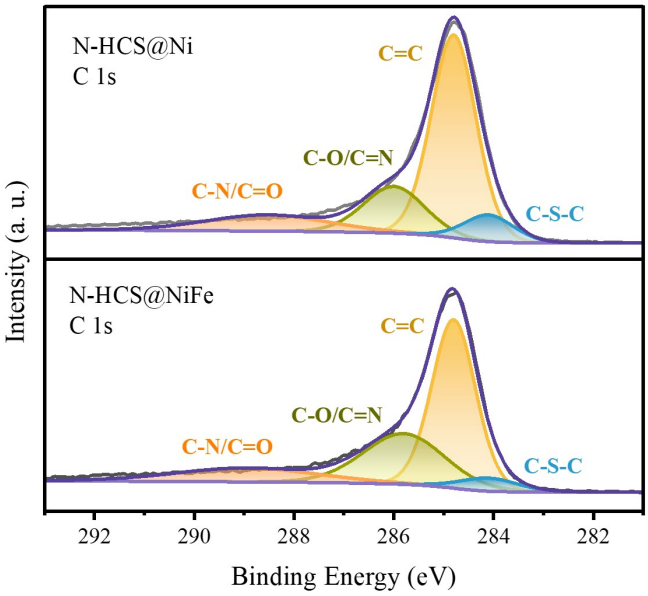

Fig. S10 High resolution XPS spectra of C 1s.

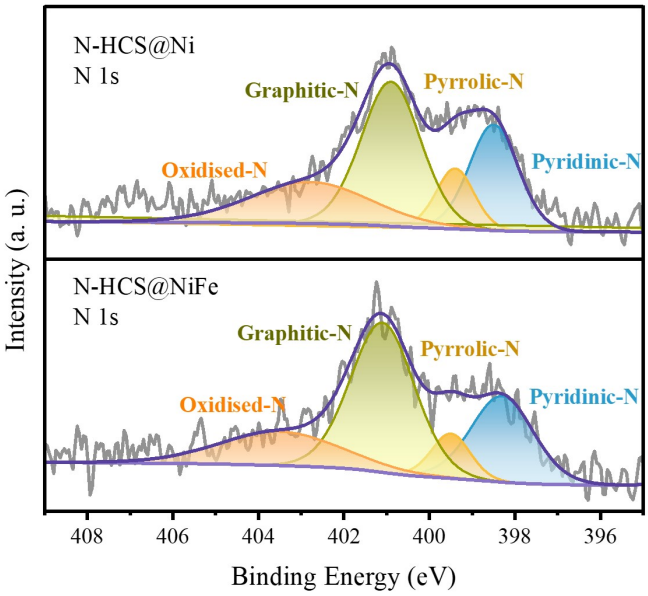

Fig. S11 High resolution XPS spectra of N 1s.

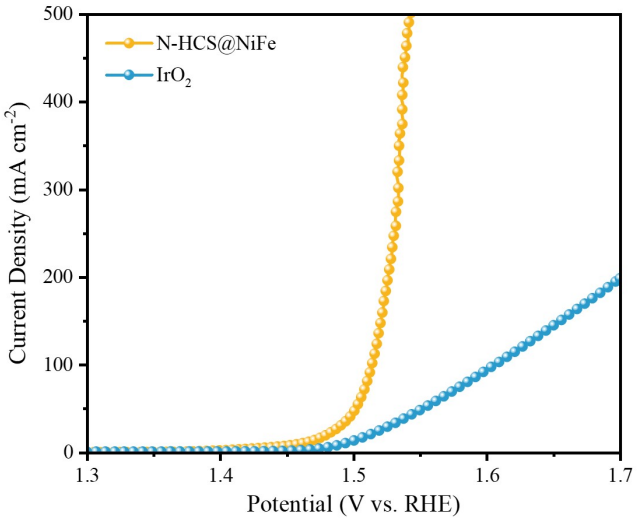

Fig. S12 (a) OER polarization curves at 2 mV s^{-1} of N-HCS@NiFe and commercial IrO_2 electrode.

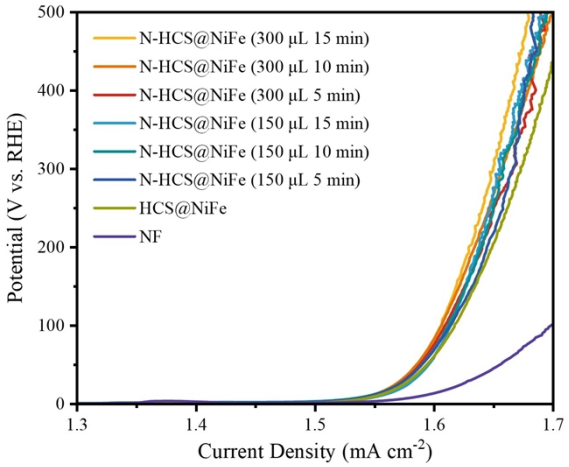

Fig. S13 LSV curves for OER at 2 mV s^{-1} of N-HCS@Ni-x-y with the amount of Ni^{2+} solution and the C_2H_2 treatment time.

As shown in **Fig. S13**, we evaluated the OER performance of the samples, and ultimately determined the precursor amount of the metal to be 300 μL and the CVD reaction time to be 15 min, labeled as N-HCS@Ni.

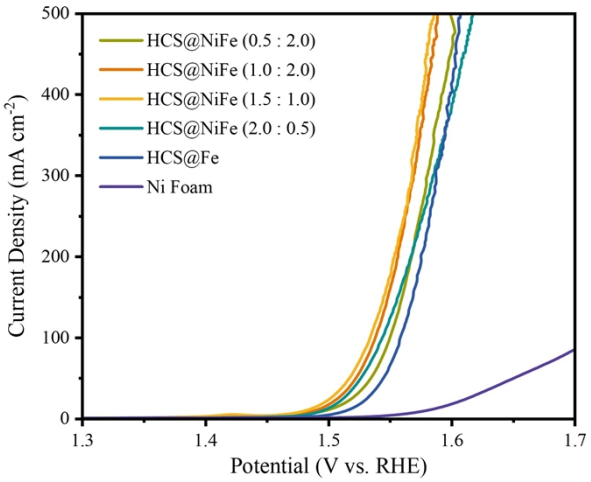

Fig. S14 LSV curves for OER at 2 mV s^{-1} of N-HCS@NiFe with the ratio of Ni and Fe in the impregnation solution.

In order to further enhance the electrocatalytic performance of the material, we introduced Fe salts into the impregnation solution and evaluated the OER performance by changing the ratio of Ni to Fe in the solution (**Fig. S14**). Finally, we also chose a ratio of Ni to Fe of 1.5:1 after comparing the electrocatalytic performance with various Ni/Fe ratio, and labeled it as HCS@NiFe. On this basis, acetylene CVD treatment was carried out for 15 min to obtain our final sample N-HCS@NiFe.

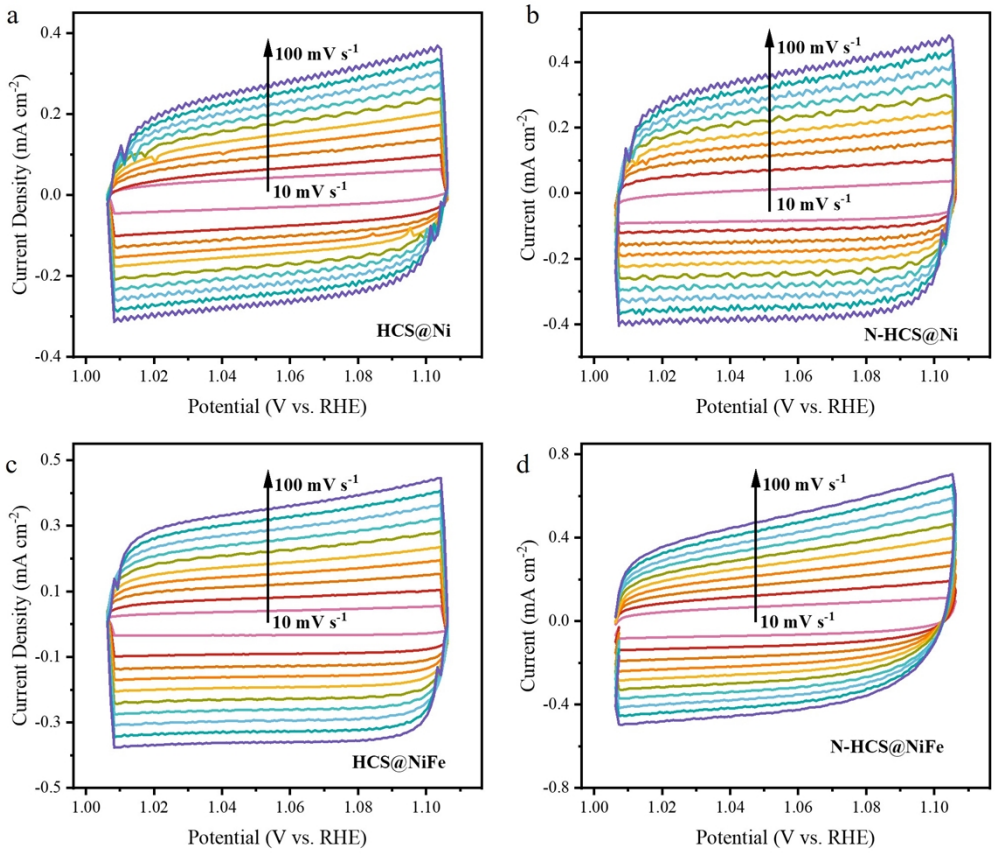

Fig. S15 CV curves of (a)HCS@Ni, (b) N-HCS@Ni, (c) HCS@NiFe and (d)N-HCS@NiFe.

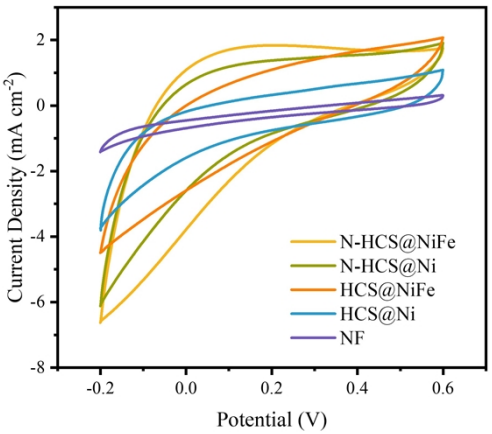

Fig. S16 CV curves of the samples scanned in PBS buffer solution between -0.2-0.6 V vs. RHE at a scan rate of 50 $mV \cdot s^{-1}$ of HCS@Ni, N-HCS@Ni, HCS@NiFe, N-HCS@NiFe and NF.

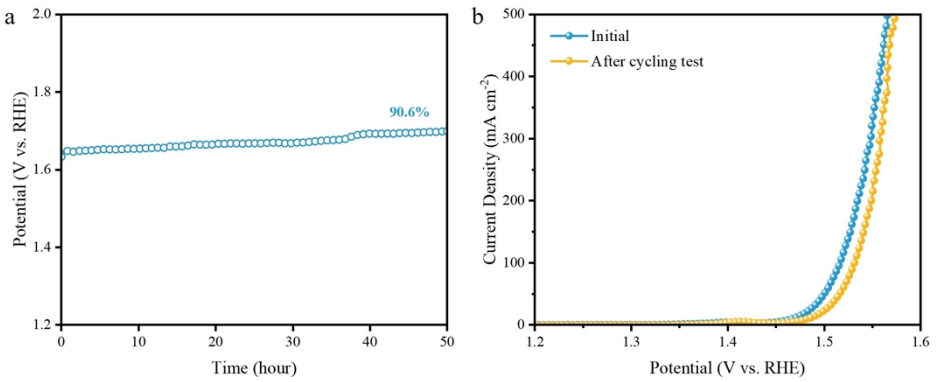

Fig. S17 Electrocatalytic stability at 300 mA cm^{-2} in 1 M KOH of HCS@NiFe.

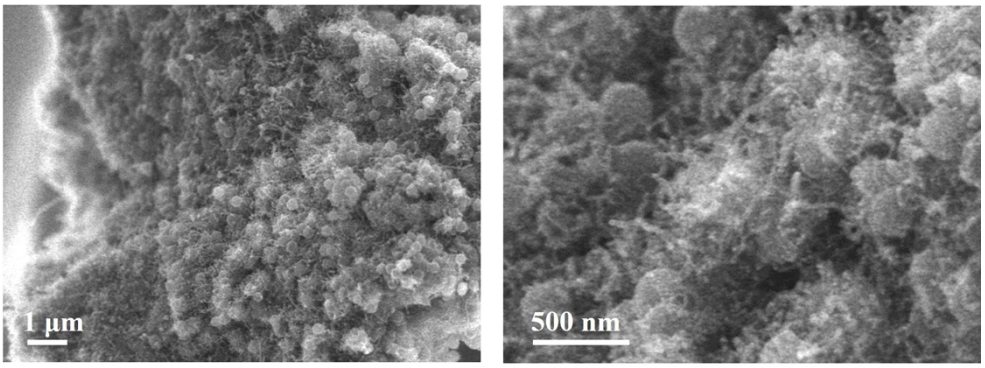

Fig. S18 SEM images of N-HCS@NiFe after long-term cycling test.

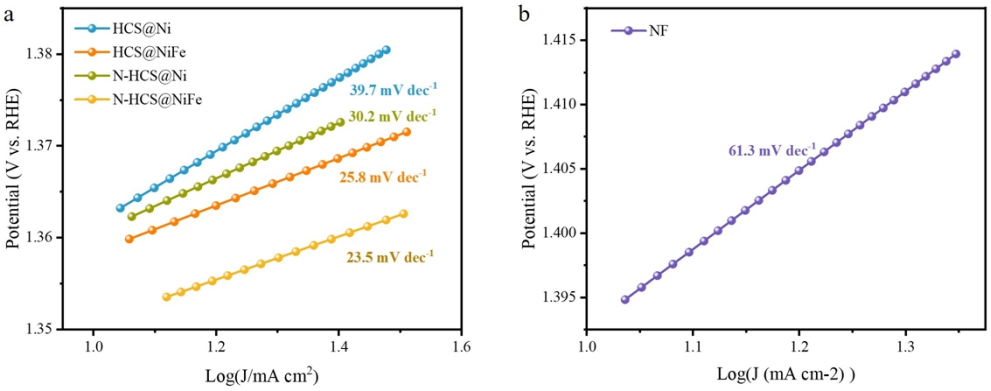

Fig. S19 Tafel slopes of (a) HCS@Ni, HCS@NiFe, N-HCS@Ni, N-HCS@NiFe and (b) NF for UOR.

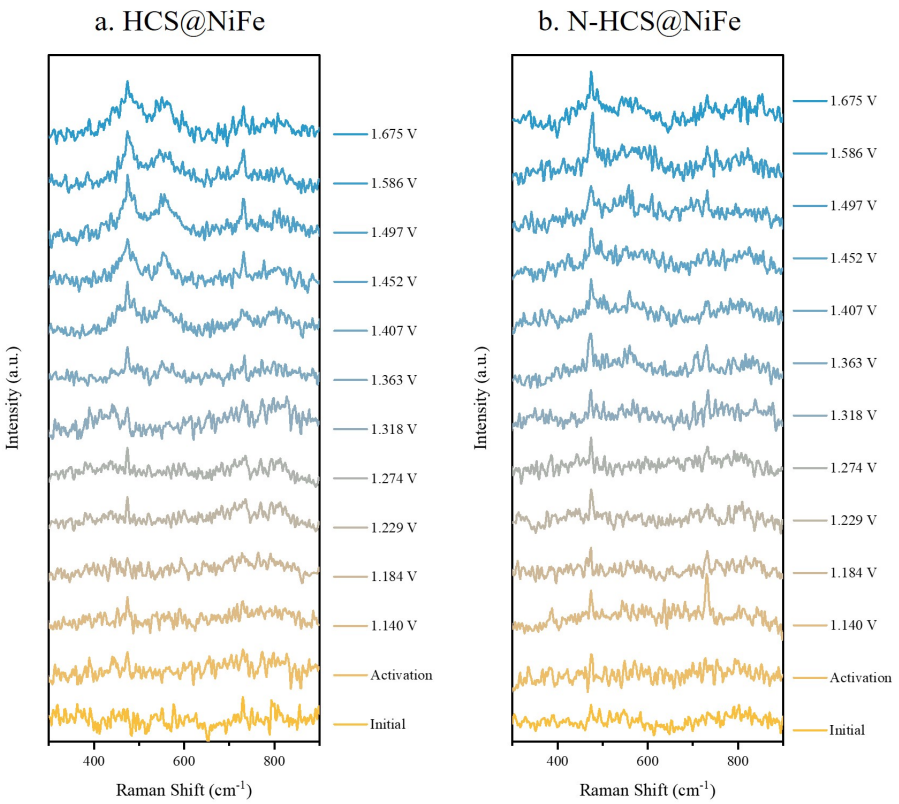

Fig. S20 In situ Raman spectra of (a) HCS@NiFe and (b) N-HCS@NiFe at various applied potentials (vs. RHE) in OER.

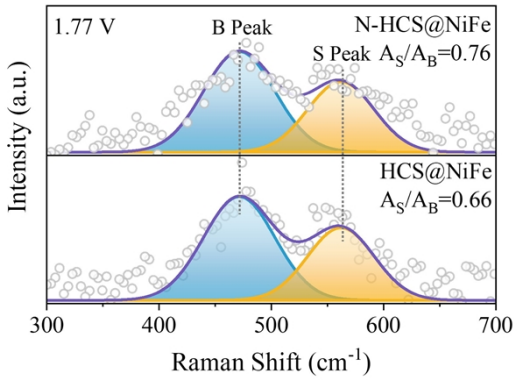

Fig. S21 Raman spectrum fitting area ratio at 1.77 V.

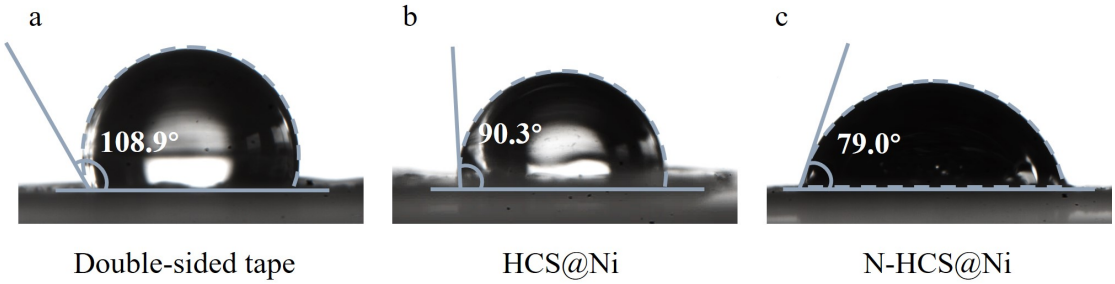

Fig. S22 Water contact angles of (a) double-sided tape; (b) HCS@Ni; (c) N-HCS@Ni.

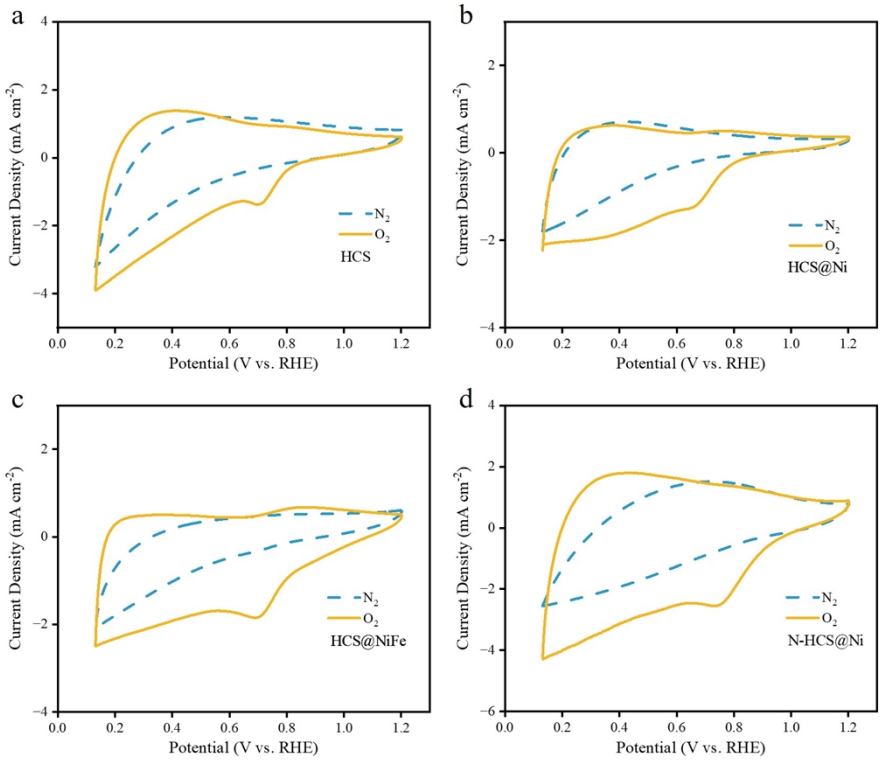

Fig. S23 CV curves of in O_2- and N_2-saturated 0.1 M KOH of (a) HCS; (b) HCS@Ni; (c) HCS@NiFe; (d) N-HCS@NiFe.

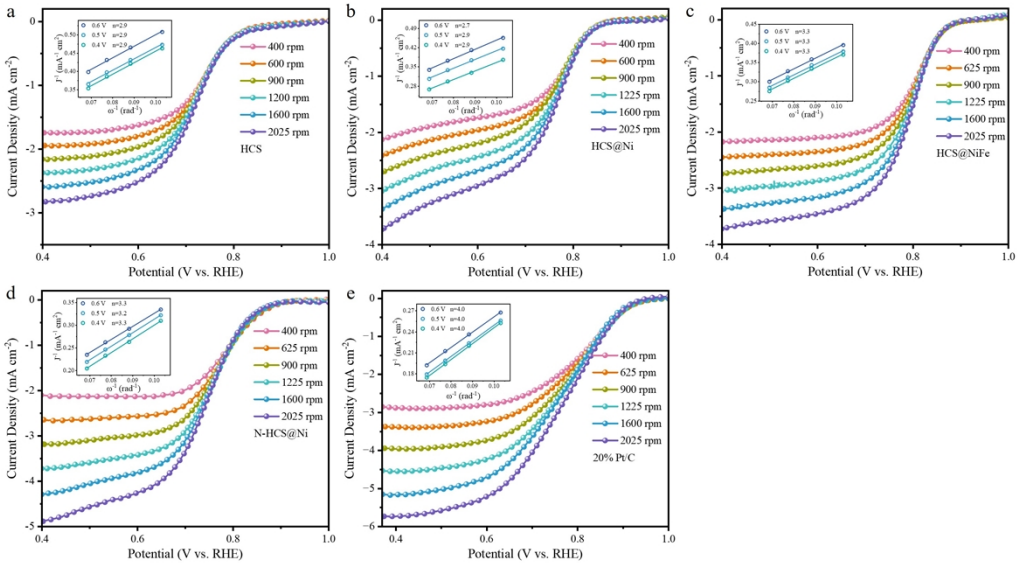

Fig. S24 ORR polarization curves under different rotation speeds and calculated number of electron transfers of (a) HCS; (b) HCS@Ni; (c) HCS@NiFe; (d) N-HCS@NiFe; (e) 20% Pt/C.

S6 Supporting Tables

Table S1 Comparison of the template methods for preparing HCS.

Template	Carbon precursor	Reaction conditions	Etching agent	References
SiO_2 spheres	phenol-formaldehyde (RF)	Stir at room temperature	HF or Hot alkali	2
Polystyrene spheres	RF	160 °C hydrothermal	High-temperature decomposition	3
ZnO spheres	RF	Stir at room temperature	HCl	4
APF (Self-template)	APF	Stir at room temperature	Acetone or Ethanol	5, 6

1. Precursor polymerization and pyrolysis process

Hollow carbon spheres (HCS) derived from phenolic resin are the subject of extensive study in the field of energy materials science, where they are regarded as a significant class of hard carbon materials due to their distinctive highly cross-linked three-dimensional structural characteristics[7].

In the synthesis of hollow carbon spheres, the template-based method, which is regarded as an efficient and commonly used phenolic resin preparation strategy, demonstrates excellent structural stability and significant confinement effects, thereby enabling precise and rigorous control of the final product morphology. For further comparison, **Table S1** summarizes various techniques for preparing HCS through template methods. Generally, rigid particles are generally used in hard-templating routes as the core template. The related hard template core can be removed, depending on their chemical nature, by calcination, dissolution, or etching, after the formation of carbon shells around the cores. Common hard template agents include SiO_2 spheres,[2] polymer spheres,[3] metal oxide nanospheres,[4] etc. The dissolution of these hard templates necessitates the utilization of corrosive/harmful etchants, and the incorporation of such templates limits the availability of scale-up production of the carbon spheres.

In relative terms, the self-template method utilizing 3-aminophenol-formaldehyde

(APF) as a carbon precursor exhibits several advantageous characteristics, including a relatively straightforward synthesis process and a low production cost. By regulating the growth kinetics of APF, a resitol with uniform external morphology but complex internal chemical composition can be generated. The internal oligomers can be dissolved by acetone[5] or ethanol[6] to form the hollow structure. In comparison to acetone etching, ethanol has a comparatively weaker solubility for APF, which can result in the formation of a loose, porous, and thick shell structure during the etching process. Additionally, the process of ethanol dissolution entails a concurrent process of regrowth. The unreacted monomers in the solution will continue to undergo polymerization on the surface of the already formed shell, thereby constructing a thicker shell structure. The dual action mechanism not only optimizes the structural properties of the material, thereby effectively increasing the overall yield, but also ensures the environmental friendliness of the raw materials and the sustainability of the entire process. After carbonization of the 3-APF spheres precursor, the retained weight percentage of the carbon sphere is up to 53 wt.%, demonstrating a high carbon retention during the carbonization process.

Therefore, due to the relatively easier scale-up fabrication process and the lower toxic/harmful etching agents usage amount, our carbon spheres synthesis process is “greener” and more environmentally friendly compare with the current exsiting methods.

2. Pickling process

In the pickling process, we used an extremely low concentration (50 mM) HCl solution with the aim of efficiently removing residual free metal ions on the material surface with minimal environmental impact. This approach not only ensures the effectiveness of the treatment, but also minimizes the generation of chemical waste, reflecting the principle of environmentally friendly green chemistry.

3. Energy consumption during CVD process

Hybridization of the 3D carbon structure with 1D CNTs can effectively enlarge the accessible surface area and form hierarchical electron transfer pathways. However, effectively fabrication of the 1D/3D CNTs/carbon sphere structure with intimate

contact area is difficult due to the aggregation of nanometal seeds during harsh treatment parameters. In the CVD process, we innovatively adopted the low-temperature CVD under 600 °C, where the pores inside the carbon spheres can effectively protect the nanoseeds from aggregation. Compared to traditional high-temperature CVD processes, this low-temperature CVD method significantly reduces the energy consumption during the entire process. More importantly, the vacuum environment effectively removes residual impurities inside the material, making low-temperature CVD process not only have a shorter operating time, but also further reduce energy consumption, demonstrating the dual advantages of high efficiency and environmental protection.

Table S2 Comparison of the OER parameters of N-HCS@NiFe with various previously reported nickel-iron-based and powder-based electrocatalysts at various current densities in 1 M KOH alkaline electrolyte.

Electrode materials	Overpotential (mV) @j (mA cm^{-2})	Tafel slope (mV dec^{-1})	Stability test (j / potential @ t)	Reference
HCS@NiFe/NF	228@10 281@100	45.7	300 mA cm^{-2}@50 h	**This work**
FeS_2 microspheres/NF	170@10 314@100	60	1.6 V vs. RHE@5 h	8
Fe_3O_4/FeS_2-2.5/NF	253@10 306@100	48	100 mA cm^{-2}@36 h	9
Fe@MoS_2-C/NF	194@10 ~303@100	63	100 mA cm^{-2}@120 h (6 M KOH)	10
Ni_2P/Fe(O)OH-40 /NF	240@10	57.25	10 mA cm^{-2}@20 h	11
H-Ni_3Fe/Ni_2Fe_2N @N-CS ANPs/CP	251@10 ~330@100	35	10 mA cm^{-2}@24 h	12
Ni0.85Se-O/CN/NF	240@10	82.5	50 mA cm^{-2}@48 h	13
NiS@FeS_2/NF	298@10	63	1.53 V vs. RHE @12 h	14
Ni/NiFeMoO_x/NF	255@10 289@100	35	1.56 V vs. RHE @24 h	15
Cu_2S@NiFe LDHs/Cu foam	286@100	57	different current densities@120 h	16
C@$NiCo_2O_4$/NF	268@10	54	10 mA cm^{-2}@20 h	17
Fe-Mo-S/Ni_3S_2@NF	~300@100	95	100 mA cm^{-2}@100 h	18
HEO/HCS-3/CP	263@10	41.24	10 mA cm^{-2}@100 h	19
Fe_2OF_4/NF	238@10	48	250 mA cm^{-2}@95 h	20
NCNT-NP@/NF	240@10	37	1.44 V vs. RHE @15 h	21
Co-P/HNCW-800-300/CG	320@10	103	~	22
NiFeMo-N_2/NF	226@10	26.7	10 mA cm^{-2}@100 h	23
Ni_2Fe_1@PANI-KOH900/GC	240@10	82	1.5 V vs. RHE @16 h	24
(Ni–Fe)S_x /NiFe(OH)$_y$/NF	290@100	58	100 mA cm^{-2}@50 h	25
NiFe(OH)$_x$@Ni_3S_2/ MoS_2-CC	309@100	39	1.5 V vs. RHE @12 h	26

Table S3 Fitting values of EIS plots corresponding to Figure 4c.

	NCS@Ni (Ω)	N-HCS@Ni (Ω)	HCS@NiFe (Ω)	N-HCS@NiFe (Ω)
$\mathbf{R_s}$	1.26	1.24	1.55	1.15
$\mathbf{R_p}$	2.85	2.72	0.156	0.0338
$\mathbf{R_{ct}}$	32.5	18.4	5.16	2.80

Table S4 Comparison of the UOR parameters of N-HCS@NiFe with various previously reported nickel-iron-based and powder-based electrocatalysts at various current densities in 1 M KOH with different concentrations of urea alkaline electrolytes.

Electrode materials	Urea concentration	Potential (V vs. RHE) @ j (mA cm^{-2})	Tafel slope (mV dec^{-1})	Stability test (j / potential @ t)	Reference
HCS@NiFe/NF	0.33 M	1.348@10 1.374@100	23.5	100 mA cm^{-2}@50 h	**This work**
CoNi-LDH/Fe MOF/NF	0.33 M	1.37@100	~	100 mA cm^{-2}@40 h	27
$CoSe_2$ HC/$CoSe_2$ NS/NF	0.5 M	1.48@100	44.5	~	28
$NiSe_2$-NiO 350/GC	0.33 M	1.33@10 1.42@100	38	1.35 V vs. RHE@2 h	29
Fe,V-NiS/NF	0.33 M	1.511@100	72.4	1.46 V vs. RHE@70 h	30
Ni CDs/CF	0.33 M	1.36@50 ~1.39@100	42.6	1.38 V vs. RHE@23 h	31
Rh/NiV-LDH/NF	0.5 M	1.33@10 1.38@100	36	20 mA cm^{-2}@40 h	32
FQD/CoNi-LDH/NF	0.5 M	1.36@10 1.42@100	17	1.40 V vs. RHE@15 h	33
CoSeP/CoP	0.5 M	1.31@20 ~1.48@100	36.5	20 mA cm^{-2}@40 h	34
Ru/FeOOH@NF	0.33 M	1.473@10	33	50 mA cm^{-2}@100 h	35
Mo-NT@NF	0.33 M	1.42@10 1.49@25	31	100 mA cm^{-2}@20 h	36
Ni-Zn ABF_3	0.33 M	1.348@10	47.1	~	37
NiFe-MIL-NH_2	0.33 M	1.398@50	14	50 mA cm^{-2}@20 h	38
$Co_2Mo_{0.2}CH$	0.33 M	1.51@10	44	10 mA cm^{-2}@40 h	39
NiF_3/Ni_2P@CC	0.33 M	1.36@10	33	10 mA cm^{-2}@10 h	40

Table S5 Comparison of the ORR parameters of N-HCS@NiFe with various previously reported nickel-iron-based electrocatalysts in 0.1 M KOH.

Electrode materials	$E_{1/2}$ (V vs. RHE)	J_L (mV cm^{-2})	Tafel slope (mV dec^{-1})	Average electron transfer number	Reference
HCS@NiFe	0.804	4.4	57.1	4.0	**This work**
Co/CNT/MCP-850	0.80	~4.8	90	3.7	[41]
FeNi-COP-800	0.803	~5.6	91	3.9	[42]
NiFeVS	0.789	~4.0	69.8	3.6	[43]
NiFe/N-CNT	0.75	~5.1	65	3.9	[44]
NiFe LDH-CNT-Co_3O_4/NC	0.79	5.79	42	4.0	[45]
porous CS	0.740	~5.8	~	4.0	[46]
Zr_2ON_2@NiFe LDH	0.64	~4.5	~	~3.2	[47]
$Mn_n(Fe_{0.3}Ni_{0.7})_{1-n}O_x$/MWCNTs-$O_x$	0.81	~4.2	~	~	[48]
PcCu-O_8-Co/CNT	0.83	5.3	60	3.93	[49]

References

1. H. Ren, Y. Pan, C. C. Sorrell and H. Du, *J. Mater. Chem. A*, 2020, **8**, 3154-3159.
2. G. Chen, X. Li, T. Zeng, R. Han and Q. Wang, *Carbon*, 2021, **171**, 464-473.
3. K. Jin, X. Li, H. Tang, Y. Shi, C. Wang, W. Guo, K. Tian and H. Wang, *Journal of Materials Science & Technology*, 2024, **177**, 224-233.
4. Z. Bai, Y. Zhang, N. Fan, C. Guo and B. Tang, *Mater. Lett.*, 2014, **119**, 16-19.
5. D.-S. Bin, Z.-X. Chi, Y. Li, K. Zhang, X. Yang, Y.-G. Sun, J.-Y. Piao, A.-M. Cao and L.-J. Wan, *Journal of the American Chemical Society*, 2017, **139**, 13492-13498.
6. Y. Pi, Y. Ma, X. Wang, C.-A. H. Price, H. Li, Q. Liu, L. Wang, H. Chen, G. Hou, B.-L. Su and J. Liu, *Adv. Mater.*, 2022, **34**, 2205153.
7. S. C. Dey, B. Worfolk, L. Lower, W. J. Sagues, M. R. Nimlos, S. S. Kelley and S. Park, *ACS Energy Lett.*, 2024, **9**, 2590-2614.
8. C. Yue, X. Zhang, J. Yin, H. Zhou, K. Liu and X. Liu, *Appl. Catal. B*, 2023, **339**, 123171.
9. M. J. Wang, X. Zheng, L. Song, X. Feng, Q. Liao, J. Li, L. Li and Z. Wei, *J. Mater. Chem. A*, 2020, **8**, 14145-14151.
10. F. Gong, M. Liu, L. Gong, S. Ye, Q. Jiang, G. Zeng, X. Zhang, Z. Peng, Y. Zhang, S. Fang and J. Liu, *Adv. Funct. Mater.*, 2022, **32**, 2202141.
11. Y. Xing, S. Liu, Y. Liu, X. Xiao, Y. Li, Z. Wang, Y. Hu, B. Xin, H. Wang and C. Wang, *Nano Energy*, 2024, **123**, 109402.
12. H. W. Choi, D. I. Jeong, S. B. Kwon, S. Woo, J. Kim, J. H. Kim, W. S. Yang, B. Lim, B. K. Kang and D. H. Yoon, *Appl. Surf. Sci.*, 2021, **566**, 150706.
13. C. Zhang, W. Xu, S. Li, X. Wang, Z. Guan, M. Zhang, J. Wu, X. Ma, M. Wu and Y. Qi, *Chem. Eng. J.*, 2023, **454**, 140291.
14. B. Jansi Rani, P. Aiswarya Kanjana, G. Ravi, R. Yuvakkumar and B. Saravanakumar, *Mater. Sci. Semicond. Process.*, 2019, **101**, 174-182.
15. Y.-K. Li, G. Zhang, W.-T. Lu and F.-F. Cao, *Adv. Sci.*, 2020, **7**, 1902034.
16. D. Guo, H. Yu, J. Chi, Y. Zhao and Z. Shao, *Int. J. Hydrogen Energy*, 2023, **48**, 17743-17757.
17. X. Wu, X. Wu, H. Lee, Q. Ye, X. Wang, Y. Zhao and L. Sun, *Energy Technol.*, 2019, **7**.
18. Y. Zhang, H. Guo, X. Li, J. Du, W. Ren and R. Song, *Chem. Eng. J.*, 2021, **404**, 126483.
19. H. He, P. Kou, Z. Zhang, D. Wang, R. Zheng, H. Sun, Y. Liu and Z. Wang, *J. Colloid Interface Sci.*, 2024, **653**, 179-188.
20. G. Zhang, Z. Li, J. Zeng, L. Yu, C. Zuo, P. Wen, Y. Liu, L. Zhong, H. Chen and Y. Qiu, *Appl. Catal. B*, 2022, **319**, 121921.
21. Y. Cheng, H. Guo, P. Yuan, X. Li, L. Zheng and R. Song, *Chem. Eng. J.*, 2021, **413**, 127531.
22. W. Zhu, W. Hu, Y. Wei, Y. Zhang, K. Pan, S. Zhang, X. Hang, M. Zheng and H. Pang, *Adv. Funct. Mater.*, **n/a**, 2409390.
23. B. C. Moon, W. H. Choi, K.-H. Kim, D. G. Park, J. W. Choi and J. K. Kang, *Small*, 2019, **15**, 1804764.

24. J. Zhang, M. Zhang, L. Qiu, Y. Zeng, J. Chen, C. Zhu, Y. Yu and Z. Zhu, *J. Mater. Chem. A*, 2019, **7**, 19045-19059.
25. Q. Che, Q. Li, Y. Tan, X. Chen, X. Xu and Y. Chen, *Appl. Catal. B*, 2019, **246**, 337-348.
26. X. H. Wang, Y. Ling, B. L. Li, X. L. Li, G. Chen, B. X. Tao, L. J. Li, N. B. Li and H. Q. Luo, *J. Mater. Chem. A*, 2019, **7**, 2895-2900.
27. Q.-N. Bian, B.-S. Guo, D.-X. Tan, D. Zhang, W.-Q. Kong, C.-B. Wang and Y.-Y. Feng, *ACS Appl. Mater. Interfaces*, 2024, **16**, 14742-14749.
28. B. Lu, Z. Li, J. Yin, K. Zhu and K. Ye, *Appl. Catal. B*, 2024, **350**, 123940.
29. Z. Liu, C. Zhang, H. Liu and L. Feng, *Appl. Catal. B*, 2020, **276**, 119165.
30. X. Feng, Y. Shi, y. Chen, Z. Xu and H. Guan, *J. Ind. Eng. Chem.*, 2022, **113**, 170-180.
31. Z. Zhu, K. Ge, Z. Li, J. Hu, P. Chen and H. Bi, *Small*, 2023, **19**, 2205234.
32. H. Sun, L. Li, H.-C. Chen, D. Duan, M. Humayun, Y. Qiu, X. Zhang, X. Ao, Y. Wu, Y. Pang, K. Huo, C. Wang and Y. Xiong, *Sci. Bull.*, 2022, **67**, 1763-1775.
33. Y. Feng, X. Wang, J. Huang, P. Dong, J. Ji, J. Li, L. Cao, L. Feng, P. Jin and C. Wang, *Chem. Eng. J.*, 2020, **390**, 124525.
34. B. Lu, C. Lv, Y. Xie, L. Gao, J. Yan, K. Zhu, G. Wang, D. Cao and K. Ye, *Small*, 2023, **19**, 2302923.
35. P. Zhao, Q. Liu, X. Yang, S. Yang, L. Chen, J. Zhu and Q. Zhang, *J. Colloid Interface Sci.*, 2024, **673**, 49-59.
36. M. Liu, W. Zou, J. Cong, N. Su, S. Qiu and L. Hou, *Small*, 2023, **19**, 2302698.
37. J. Xie, R. Ding, Y. Li, J. Guo, Y. Zhang, Q. Fang, M. Yan, Y. He, Z. Yan, Z. Chen, X. Guo, Q. Yang, J. Luo, Y. Zhang, X. Sun and E. Liu, *Nano Energy*, 2024, **126**, 109669.
38. Z. Gao, Y. Wang, L. Xu, Q. Tao, X. Wang, Z. Zhou, Y. Luo, J. Yu and Y. Huang, *Chem. Eng. J.*, 2022, **433**, 133515.
39. S. Zheng, H. Qin, X. Cao, T. Wang, W. Lu and L. Jiao, *J. Energy Chem.*, 2022, **70**, 258-265.
40. K. Wang, W. Huang, Q. Cao, Y. Zhao, X. Sun, R. Ding, W. Lin, E. Liu and P. Gao, *Chem. Eng. J.*, 2022, **427**, 130865.
41. X. Zhou, X. Liu, J. Zhang, C. Zhang, S. J. Yoo, J.-G. Kim, X. Chu, C. Song, P. Wang, Z. Zhao, D. Li, W. Zhang and W. Zheng, *Carbon*, 2020, **166**, 284-290.
42. Z. Liao, Y. Wang, Q. Wang, Y. Cheng and Z. Xiang, *Appl. Catal. B*, 2019, **243**, 204-211.
43. F. N. I. Sari, Y.-C. Lai, Y.-J. Huang, X.-Y. Wei, H. Pourzolfaghar, Y.-H. Chang, M. Ghufron, Y.-Y. Li, Y.-H. Su, O. Clemens and J.-M. Ting, *Adv. Funct. Mater.*, 2024, **34**, 2310181.
44. H. Lei, Z. Wang, F. Yang, X. Huang, J. Liu, Y. Liang, J. Xie, M. S. Javed, X. Lu, S. Tan and W. Mai, *Nano Energy*, 2020, **68**, 104293.
45. T.-E. Ko, S. Hosseini, C.-M. Tseng, J.-E. Tsai, W.-H. Wang and Y.-Y. Li, *J. Taiwan Inst. Chem. Eng.*, 2022, **136**, 104397.
46. C. Su, Y. Liu, Z. Luo, J.-P. Veder, Y. Zhong, S. P. Jiang and Z. Shao, *Chem. Eng. J.*, 2021, **406**, 126883.

47. X. Hu, W. Tian, Z. Wu, X. Li, Y. Li and H. Wang, *J. Colloid Interface Sci.*, 2024, **672**, 610-617.
48. D. M. Morales, M. A. Kazakova, S. Dieckhöfer, A. G. Selyutin, G. V. Golubtsov, W. Schuhmann and J. Masa, *Adv. Funct. Mater.*, 2020, **30**, 1905992.
49. H. Zhong, K. H. Ly, M. Wang, Y. Krupskaya, X. Han, J. Zhang, J. Zhang, V. Kataev, B. Büchner, I. M. Weidinger, S. Kaskel, P. Liu, M. Chen, R. Dong and X. Feng, *Angew. Chem. Int. Ed.*, 2019, **58**, 10677-10682.